Chinese Chemical Letters 37 (2026) 111427

Contents lists available at ScienceDirect

Chinese Chemical Letters

journal homepage: www.elsevier.com/locate/cclet

Tungsten oxide quantum dot-based supramolecular assembly with tunable photochromic kinetics towards time-encoded anti-counterfeiting

Xiaojian Yan[a,b], Saijin Huang[b], Wenfeng Liu[b], Li-Li Tan[b], Gaobin Wang[c], Liping Cao[d], Li Shang[a,b,*]

[a] Shenzhen Research Institute of Northwestern Polytechnical University, Shenzhen 518057, China
[b] State Key Laboratory of Solidification Processing, School of Materials Science and Engineering, Northwestern Polytechnical University, Xi'an 710072, China
[c] Queen Mary University of London Engineering School, Northwestern Polytechnical University, Xi'an 710072, China
[d] Key Laboratory of Synthetic and Natural Functional Molecule of the Ministry of Education, College of Chemistry and Materials Science, Northwest University, Xi'an 710069, China

ARTICLE INFO

Article history:
Received 28 March 2025
Revised 15 May 2025
Accepted 6 June 2025
Available online 7 June 2025

Keywords:
Tungsten oxide quantum dots
Anti-counterfeiting
Photochromic kinetics
Supramolecular assembly

ABSTRACT

The development of advanced anti-counterfeiting technology using photochromic inorganic materials with dynamic optical signals has garnered significant interest, but the limited color response and uncontrolled photochromic kinetics largely restrict their practical application. In this work, we report the design of photochromic supramolecular assembly based on host-guest chemistry, enabling kinetics-tunable time-encoded anti-counterfeiting. By co-assembling of photochromic tungsten oxide quantum dots (WO_3 QDs) with cucurbit[7]uril (CB[7]), we developed a kinetics-tunable photochromic supramolecular assembly (WO_3–CB[7]). The WO_3–CB[7] assembly exhibits distinct photochromic kinetics compared to free WO_3 QDs due to efficient suppression of photogenerated decomposition of water adsorbed on WO_3 QDs, as verified by spectral and photophysical analysis. The photochromic kinetics can be readily modulated by adjusting the WO_3 QDs to CB[7] ratio. The kinetics-tunable photochromic WO_3–CB[7] assembly has been successfully applied as innovative anti-counterfeiting materials for fabricating time-encoded anti-counterfeiting arrays and information encryption system. The irradiation time serves as a key parameter for decrypting the final information, thereby enhancing the complexity of replication and counterfeiting. This approach offers a simple, scalable and generalizable strategy for designing advanced optical anti-counterfeiting materials by integrating inorganic photochromic materials with the supramolecular strategy.

© 2025 Published by Elsevier B.V. on behalf of Chinese Chemical Society and Institute of Materia Medica, Chinese Academy of Medical Sciences.

The global proliferation of counterfeit currencies, luxury goods, documents, and pharmaceuticals highlight the urgent need for innovative and sophisticated anti-counterfeiting technologies. Stimuli-responsive materials, which exhibit reversible color changes under external stimuli such as thermal, stress, light, electricity, and magnetism, have shown great promise for developing advanced anti-counterfeiting strategies [1–5]. Among these, photochromic materials that utilize light as a stimulus offer significant practical advantages, including ease of operation and non-contact control [6–10]. To date, organic photochromic dyes (*e.g.*, spiropyran, diarylethene, and azobenzene) have been extensively exploited for various anti-counterfeiting applications [11–16]. However, their widespread use in high-performance optical devices has been limited by poor thermal stability, weak fatigue resistance, and complex synthesis processes. In contrast, inorganic photochromic materials typically exhibit excellent thermal stability, long-term cycling durability, and superior chemical resistance [17–19], making them increasingly attractive for anti-counterfeiting applications in recent years.

To date, researchers have developed a series of inorganic photochromic materials (*e.g.*, transitional metal oxides, rare earth doped compounds and metal halides) for anti-counterfeiting applications based on their reversible optical coloring/bleaching characteristics [20–23]. For example, Chen *et al.* [24] fabricated sustainable rewritable paper by directly grafting amino-modified tung-

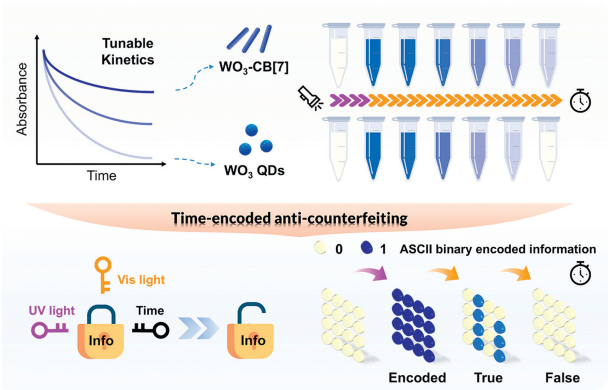
* Corresponding author at: State Key Laboratory of Solidification Processing, School of Materials Science and Engineering, Northwestern Polytechnical University, Xi'an 710072, China.
E-mail address: li.shang@nwpu.edu.cn (L. Shang).

https://doi.org/10.1016/j.cclet.2025.111427
1001-8417/© 2025 Published by Elsevier B.V. on behalf of Chinese Chemical Society and Institute of Materia Medica, Chinese Academy of Medical Sciences.

sten oxide quantum dots (WO_3 QDs) onto cellulose papers. This rewritable paper exhibits high color contrast, long color-retention and good rewritability, making it suitable for application in anti-counterfeiting, encryption, and decryption. Cao *et al.* [25] also designed a type of rewritable paper with an ultra-high color contrast through inducing oxygen vacancy defects in $Ba_3MgSi_2O_8:Pr^{3+}$, which show reversible optical/thermal response and excellent color reversibility. However, the narrow range of color changes in traditional inorganic materials can be easily duplicated, which has increasingly become inadequate in addressing the growing issues of counterfeiting. To tackle this challenge, researchers have attempted to couple inorganic materials with other functional motifs aiming to achieve multi-level anti-counterfeiting. For instance, Feng *et al.* [26] reported photoswitchable printing based on $WO_{2.9}$ nanoparticle-doped shape memory polymer composites with controlled photothermal property through selective light absorption. The incorporation of photochromic $WO_{2.9}$ nanoparticles allows for reversibly photoswitchable, spatial and remote control of shape morphing, expanding the potential application of photo-triggered shape-morphing structures. Nevertheless, this strategy inevitably complicates both the synthesis and operation procedures, which may also impact the photochromic property of inorganic materials. Hence, it is crucial to further develop alternative, simple yet efficient strategies to address the challenges of inorganic photochromic materials for advanced optical applications.

Recently, host-guest chemistry based on the noncovalent supramolecular interactions has offered promising avenues for developing advanced anti-counterfeiting technologies [27–32]. For example, by confining to the cavity of β-cyclodextrin (β-CD) *via* host-guest chemistry, the fluorescence of butyl–naphthalimide with flexible ethylenediamine-functionalized β-CD (N–CD) is significantly diminished [33], which can be recovered by a competing guest molecule. Based on this responsiveness, N–CD has been employed as a fluorescent, responsive ink for encoding information onto polymer brushes that are grafted with dangling adamantane groups on responsive hydrogels. However, there are few reports leveraging supramolecular interactions to manipulate photochromic properties of inorganic materials, especially for the construction of sophisticated anticounterfeiting systems. Herein, we report the design of kinetics-tunable photochromic supramolecular assembly based on WO_3 QDs towards time-encoded anti-counterfeiting. In this study, WO_3 QDs were chosen as the model inorganic photochromic materials owing to their easy synthesis, good photostability and low cost [34–39]. Host-guest assembly with tunable photochromic kinetics was fabricated by precisely adjusting the ratio of WO_3 QDs to cucurbit[7]uril (CB[7]), based on which dynamic optical anti-counterfeiting can be achieved. Moreover, the photochromic WO_3–CB[7] assembly was incorporated with agarose hydrogels for fabricating patch-type flexible anti-counterfeiting materials, demonstrating their great potential for practical applications (Scheme 1).

WO_3 QDs protected by polyvinyl pyrrolidone (PVP) were first synthesized *via* a hydrothermal reaction [40], as illustrated in Fig. 1A. Transmission electron microscopy (TEM) images of WO_3 QDs revealed a *quasi*-spherical shape with an average diameter of 1.8 ± 0.3 nm (Fig. 1B). CB[7] was chosen as the model macrocycle molecule owing to its distinct binding affinity, excellent solubility and hydrophobic cavity [41–43]. Subsequently, the WO_3–CB[7] assembly was formed by simply mixing WO_3 QDs with CB[7] in aqueous solution, resulting in a white suspension. The obtained WO_3–CB[7] possess a hydrodynamic diameter of 1.0 ± 0.1 μm, which is much larger than that of WO_3 QDs (2.4 ± 0.2 nm) only, as revealed by the dynamic light scattering (DLS) measurement (Fig. 1C), indicating the formation of large-sized assembly. In addition, TEM images further showed that the resulted WO_3–CB[7] exhibits a rod-like shape with mean length



Scheme 1. Schematic diagram of WO_3 QD-based supramolecular assembly with tunable photochromic kinetics for time-encoded anti-counterfeiting.

and diameter of 2.5 and 0.6 μm, respectively (Fig. 1D and Fig. S1A in Supporting information), possessing a length-diameter ratio of 4.2 (Fig. S1B in Supporting information). Further analysis by high-angle annular dark field scanning transmission electron microscopy (HAADF-STEM) image and corresponding elemental mapping images (Fig. 1E) also showed a significant degree of elemental overlap for N, O and W, confirming the homogeneous distribution of WO_3 QDs in the composites.

Additionally, the absorption of WO_3 QDs in the visible region increased significantly after co-assembly with CB[7] owing to the scattering effect (Fig. 1F), which is consistent with the formation of large-size rod-like WO_3–CB[7] assembly. Moreover, the intrinsic fluorescence intensity of WO_3 QDs decreased gradually with raising the concentration of CB[7] in the solution (Fig. S2 in Supporting information), confirming the interactions between WO_3 QDs and CB[7]. By fitting the fluorescence quenching data with a Stern-Volmer equation [44], the quenching constant K_{sv} was calculated as 6.8×10^2 L/mol, suggesting a mild quenching efficiency [45,46]. Furthermore, the fluorescence lifetime of WO_3 QDs kept unchanged after assembling with CB[7] (Fig. 1G), suggesting the static fluorescence quenching of WO_3 QDs by CB[7], further confirming the formation of WO_3–CB[7] assembly.

In order to evaluate the photochromic performance of WO_3–CB[7] assembly, we first studied their coloring behavior by absorption spectroscopy. As shown in Fig. 2A, WO_3–CB[7] assembly exhibits strong absorption in the visible region without distinct peaks, which can be attributed to the scattering effect of large-size rod-like assembly. Upon irradiation with UV light, a strong absorption band in the range of 500–800 nm appeared with the maximum locating at 635 nm within seconds, similar as that of free WO_3 QDs [40]. Meanwhile, this photochromic behavior could be visualized by the obvious color change of the suspension from white to dark blue. The well-retained photochromic property of WO_3–CB[7] assembly suggests that the complexion with CB[7] does not affect the coloring feature of WO_3 QDs. Upon further irradiation with visible light, the color of the suspension gradually faded as expected. The contrast ratio was nearly 100 % based on complete optical bleaching achieved within 10 min of visible light exposure for both systems.

To investigate the influence of CB[7] on the photochromic process of WO_3 QDs in the assembly, *in-situ* photochromic kinetics measurements were conducted under continuous UV light and further visible light irradiation. The concentration of WO_3 QDs in all composites was set as 1.5 mg/mL, and the absorbance at 635 nm before UV irradiation was set as the baseline to rule out the contribution from the scattering effect. For coloring process, as shown in Fig. S3 (Supporting information), after UV irradiation for 1 min, the absorbance of WO_3 QDs at 635 nm exhibited a slight increase

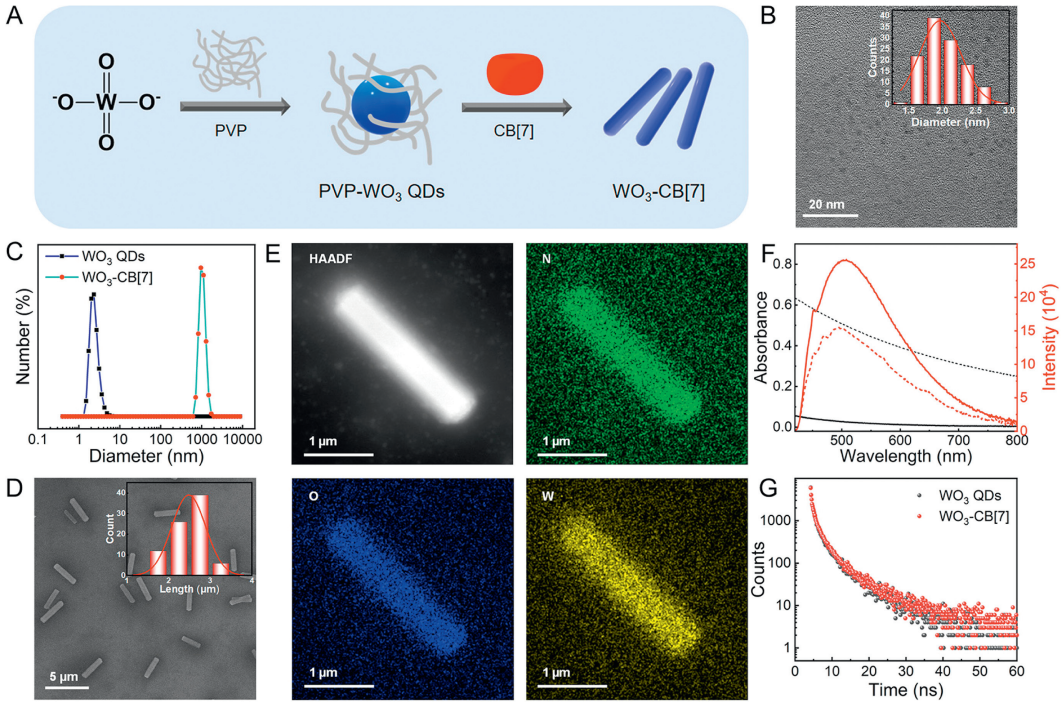


Fig. 1. (A) Synthesis route of WO_3–CB[7] assembly. (B) TEM images of WO_3 QDs (insert: corresponding diameter distribution histogram of WO_3 QDs). (C) DLS curves of WO_3 QDs and WO_3–CB[7]. (D) SEM images of WO_3–CB[7] (insert: corresponding length distribution histogram of WO_3–CB[7]). (E) HAADF-STEM image and corresponding elemental mappings of WO_3–CB[7]. (F) Absorption spectra (black line) and fluorescence emission spectra (red line, excitation wavelength: 365 nm) of WO_3 QDs (solid line) and WO_3–CB[7] assembly (dotted line). (G) Fluorescence decay curves of WO_3 QDs and WO_3–CB[7] assembly (excitation wavelength: 405 nm).

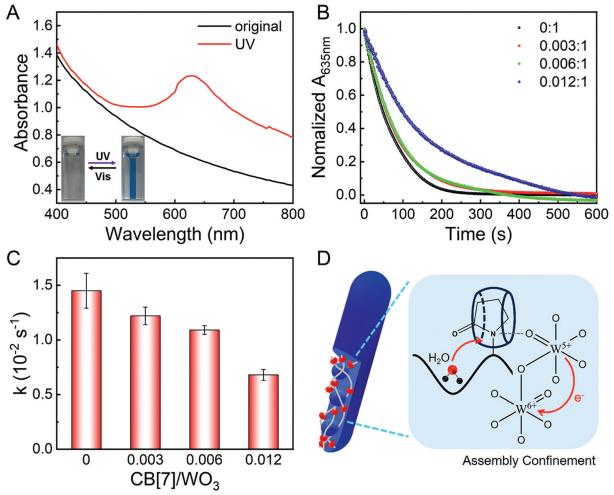


Fig. 2. (A) Absorption spectra of WO_3–CB[7] assembly before and after UV light irradiation (insert: photos of WO_3–CB[7] aqueous solution upon UV–vis light irradiation). (B) Changes of the absorbance of WO_3 QDs and WO_3–CB[7] with different molar ratios at 635 nm under visible light irradiation for varied times after UV irradiation for 1 min. (C) Comparison of the bleaching rates of WO_3 QDs and WO_3–CB[7] assembly with different molar ratios at 635 nm under visible light irradiation upon fitting the data with the first-order kinetics. (D) Schematic representation of the transfer of photogenerated electrons in WO_3–CB[7] assembly.

upon complexation with CB[7]. Meanwhile, as the concentration of CB[7] increased, the absorbance decreased slightly, indicating a reduction of coloring efficiency. This can be attributed to the formation of large-size assembly, which limits the contact between WO_3 QDs and the adsorbed H_2O molecule [24,35]. However, further increase of the CB[7]/WO_3 ratio led to a recovery in the coloring efficiency, suggesting a possible change of the assembly structure at higher ratios.

Quantitative analysis was then applied to further analyze the influence of CB[7] on the bleaching kinetics of WO_3 QDs, wherein the absorbance at 635 nm after 1 min UV irradiation was normalized for a better comparison. Both WO_3 QDs and the WO_3–CB[7] assembly exhibited comparable photochromic kinetics under UV irradiation conditions: 0.1 s for the response time (defined as time to 10 % saturation) and 30 s for saturation time (Fig. S4 in Supporting information). As shown in Fig. 2B and Fig. S5 (Supporting information), the results revealed that the absorbance change of WO_3 QDs and WO_3–CB[7] assembly with different molar ratios at 635 nm follows the first-order kinetics. As the CB[7]/WO_3 ratio increased, the average bleaching rate of WO_3 QDs decreased dramatically from 1.45×10^{-2} s^{-1} to 0.90×10^{-2} s^{-1} (Fig. 2C). Further increasing the CB[7]/WO_3 ratio would cause obvious decrease of the coloring efficiency as well as deviation from the first-order reaction kinetics (Fig. S6 in Supporting information). Therefore, a CB[7]/WO_3 ratio of 0.012 was adopted in the following study. Moreover, the decrease in the kinetics rate can be partially reversed by introducing competitive guest molecules (*e.g.*, amantadine, AD), although this addition may slightly impact the photochromic property of WO_3 QDs (Fig. S7 in Supporting information). Previous reports showed that the adsorbed H_2O molecule on the materials also play a vital role in the photochromism of WO_3 QDs [17,35]. Upon UV irradiation, electrons (e^-) and holes (h^+) are generated. The h^+ can weaken the H–O bond strength of the adsorbed H_2O and decompose it into protons and oxygen radicals. Subsequently, the protons together with the photogenerated e^- react with WO_3, leading to the formation of blue-colored hydrogen tungsten bronze. As a result, a white to blue color change is achieved in WO_3 QDs. Particularly, the absorbed H_2O molecule on the surface of WO_3 QDs by the ligand (*i.e.*, PVP) serves as effective proton donors to form colored hydrogen-based compounds and leads to the color change, which can improve the photochromic responses. For WO_3–CB[7] assembly, abundant CB[7] molecules are assembled around WO_3 QDs, which bear a rigid and hydrophobic cavity [41,47], limiting the decomposition

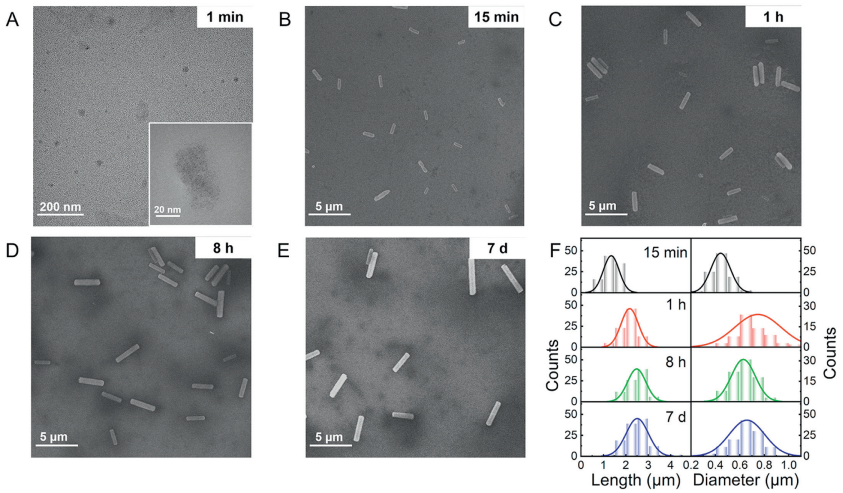


Fig. 3. (A) TEM image of the intermediate products collected after WO_3 QDs and CB[7] reacting for 1 min (inset: high-magnification TEM image of a representative WO_3–CB[7] assembly). (B-E) Representative SEM images of the intermediate products collected during the formation of WO_3–CB[7] after reacting for different times. (F) Histogram of the corresponding length and diameter distribution of WO_3–CB[7].

of absorbed water by h^+ (Fig. 2D). Consequently, the photochromic response of WO_3 QDs is retarded in the WO_3–CB[7] composites.

To explore the assembly mechanism of WO_3–CB[7] complex, we first investigated its morphological evolution at different time intervals by electron microscopy. As shown in Fig. 3A, after mixing WO_3 QDs with CB[7] for 1 min, irregular and heterogeneous aggregates appeared in TEM image. Notably, dark-colored nanodots were observed in the assembly from the high-resolution TEM image, confirming the successful nucleation with the assembly of WO_3 QDs by CB[7]. Within 15 min, these irregular assemblies evolved into regular rod-like morphology with mean length and diameter of 1.3 and 0.4 μm, respectively, exhibiting a length-diameter ratio of 3.3 (Fig. 3B). As time progressed, these rod-like assemblies grew up gradually until achieving the final morphology after 8 h (Figs. 3C-E). During this process, the length of the assembled rod increased continuously (Fig. 3F), while the diameter almost kept unchanged after 1 h, resulting in a longitudinal extension of the final assembly. Moreover, we note that the assembly with different CB[7]/WO_3 ratios show different assembly morphology. As shown in Figs. S8-S11 (Supporting information), a lower CB[7]/WO_3 ratio (*e.g.*, 0.006) leads to a thinner rod-like morphology, while increasing the ratio (*e.g.*, 0.05) will lead to a morphological transformation from rods into cubes. The morphological change is closely related to the above-mentioned kinetics processes. For instance, the rod-like morphology formed at low CB[7]/WO_3 ratios may indicate a more effective inhibition in the decomposition of absorbed water by h^+. Conversely, at high ratios, the cube-like morphology can re-establish this restriction. In summary, regulating the WO_3/CB[7] ratio can yield assembly with different structures, which in turn exhibit significantly different, adjustable photochromic kinetic property. This provides a new strategy for precisely controlling the photoresponsive process of WO_3-based photochromic materials.

Isothermal titration calorimetry (ITC) was further performed to study the thermodynamic characters of the supramolecular host-guest complexation between WO_3 QDs and CB[7]. As shown in Fig. 4A, the fitting curve of the titration data confirmed a 1:2.86 binding mode (the *n*-value is measured as 0.35) between CB[7] and WO_3 QDs (based on the molar concentration of W element). The overall binding constant (K_a) was calculated to be 5.84×10^4 L/mol, indicating a strong affinity between the host and guest molecules in water [48,49]. The binding forces likely include hydrogen bonding and van der Waals force, as deduced from the favorable enthalpic contribution (ΔH: −17.1 kcal/mol) and negative entropy change [50]. To verify the interaction sites between WO_3 QDs and CB[7], Fourier transform infrared spectroscopy (FTIR) was then employed. As shown in Fig. S12 (Supporting information), peaks at around 965 cm^{-1} and 891 cm^{-1}, which are assigned to W=O terminal mode and W-O-W bridging mode of WO_3 QDs, respectively, did not shift after assembling with CB[7]. This suggests that no new covalent bond formed between WO_3 QDs and CB[7]. Meanwhile, the C=O stretching vibration peak (1660 cm^{-1}) of PVP, ligand of WO_3 QDs, moved to higher wavenumber (1729 cm^{-1}), indicating the formation of hydrogen bonds between PVP and CB[7], and the decrease of the surrounding environmental polarity of PVP [51,52].

The chemical state of W in the assembly was studied by high resolution X-ray photoelectron spectra (XPS). As shown in Fig. S13 (Supporting information), the signal of W 4f in WO_3–CB[7] assembly can be deconvoluted into two strong bands of W^{5+} at 36.5 eV ($4f_{5/2}$) and 34.2 eV ($4f_{7/2}$), and two weak bands of W^{6+} at 37.8 eV ($4f_{5/2}$) and 35.6 eV ($4f_{7/2}$), similar as that of free WO_3 QDs. The atomic percentage of W^{5+} and W^{6+} in WO_3–CB[7] assembly was calculated to be *ca.* 20 % and 80 %, respectively. Thus, the O/W atomic ratio of WO_3 QDs in WO_3–CB[7] assembly is approximately 2.9, which is the same as that of free WO_3 QDs. This result confirms the presence of oxygen vacancy, which is vital for the photochromic property of WO_3 QDs [53,54], suggesting that complexion with CB[7] did not change the internal chemical structure of WO_3 QDs.

The detailed structure of WO_3–CB[7] assembly was further studied by small-angle X-ray scattering (SAXS). As shown in Fig. 4B, WO_3–CB[7] displayed a broad peak centering at 1.9 nm, aligning with the diameter of individual WO_3 QDs. Pair distance distribution function (PDDF) analysis was further implemented to obtain more information of the WO_3–CB[7] assembly based on the following functions [53]:

$$p(r) = \frac{r}{2\pi^2} \int_0^\infty sI(s) \sin(sr) ds \quad (1)$$

$$s = (4\pi \sin\theta)/\lambda \quad (2)$$

where *p(r)* and *I(s)* are PDDF and its Fourier transform, respectively. *s* is calculated based on function (2), in which 2θ is the angle between the scattered and the incident radiation, and λ is

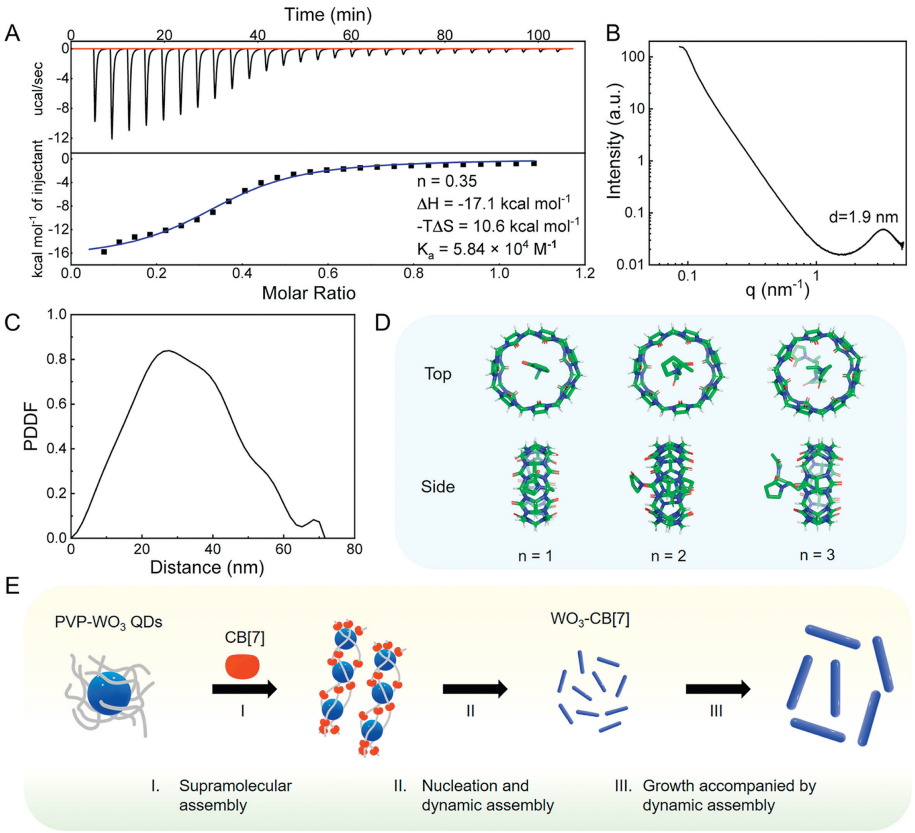


Fig. 4. (A) ITC result for the binding between WO_3 QDs and CB[7] in aqueous solution. (B) SAXS result of WO_3–CB[7] assembly. (C) PDDF profile obtained from the corresponding fitting result. (D) Visualization of molecular docking results of PVP (with different degrees of polymerization: $n = 1, 2, 3$) with CB[7] by PyMOL software. (E) Proposed formation process of WO_3–CB[7] assembly.

the wavelength. With the assistance of *ATSAS 3.0* [55], final PDDF profile can be obtained. As shown in Fig. 4C, the curve exhibits a broad peak with trailing tails, which agrees with the characteristic curve of the rod-like morphology [56,57]. Notably, D_{max}, which is the largest dimension of the assembly, was calculated as 72 nm. In addition, the prominent characteristic peaks located at 27 nm. Both values are likely the scale of the axial length and diameter of dominated rod-like assemblies, respectively. Indeed, this corresponds to a length-to-diameter ratio of *ca.* 2.7, which agrees well with the morphology observed *via* SEM images before 1 h. Moreover, two shoulder peaks at 40 nm and 55 nm could be observed in Fig. 4C, indicating a heterogeneous size distribution of the assembly at nanoscale. These results also suggest a nucleation-growth-reaggregation process during the assembly of WO_3–CB[7].

Molecular docking was further employed to elucidate the interactions between WO_3 QDs and CB[7]. In this study, WO_3 QDs were encapsulated by PVP as the ligand, which is a linear long chain polymer. To simplify the docking process, PVP with three different degrees of polymerization ($n = 1, 2, 3$) was set as the example to dock with CB[7] using AutoDock Vina method [58]. The output from AutoDock was further analyzed using PyMOL software [59]. As shown in Fig. 4D, the five-membered ring of the PVP's side group can easily enter the cavity of CB[7] to trigger the assembly process. Notably, the absence of hydrogen bonding in the docking results may be attributed to rather weak interactions between PVP and CB[7] without WO_3 QDs. Moreover, though a higher degree of polymerization may lead to the fold of long chain in PVP, the docking result suggests that only one five-membered ring of the PVP side group can enter the cavity of CB[7] because of the steric hindrance effect [60,61]. This indicates that the assembly of WO_3 QDs with CB[7] tends to extend along the backbone of PVP. Meanwhile, the assembly of CB[7] with WO_3 QDs capped by PVP with different molecular weights was synthesized. As shown in Fig. S14 (Supporting information), WO_3 QDs capped by PVP with a lower molecular weight (K15, MW: 8000–12,000) tended to form WO_3–CB[7] assembly with a cube-like morphology, while a higher molecular weight (K60, MW: 270,000–400,000) of PVP led to the formation of disordered assembly. These facts further confirmed the ligand-dependent assembly of WO_3 QDs and CB[7].

Based on the above results, the formation process of WO_3–CB[7] is proposed, as illustrated in Fig. 4E. Firstly, WO_3 QDs assemble with CB[7] *via* supramolecular interactions (*i.e.* hydrogen bonding and van der Waals force), generating irregular and heterogeneous assemblies. Secondly, nucleation of WO_3–CB[7] and dynamic assembly of WO_3 QDs along the backbone of PVP occur as the reaction proceeds. Finally, WO_3–CB[7] grows outward, leading to the formation of uniform rod-like assemblies until achieving equilibrium. Importantly, the assembly of WO_3 QDs through hydrophobic cavity of CB[7] *via* host-guest chemistry also restricts the decomposition of absorbed water by h^+ on the surface of WO_3 QDs, thus reducing the photochromic response rate of WO_3 QDs in the WO_3–CB[7] composites.

Encouraged by the distinct photo-responsive property of WO_3–CB[7] assembly, its potential application for time-encoded anti-counterfeiting and information encryption was investigated. Taking advantage of the kinetics-tunable photochromic property, the WO_3–CB[7] assembly can be directly used for fabricating time-encoded anti-counterfeiting array. Herein, free WO_3 QDs without the kinetics-tunable property were also used together as a control. In this anti-counterfeiting mode, the final de-coding information can only be obtained by combining the proper light irra-

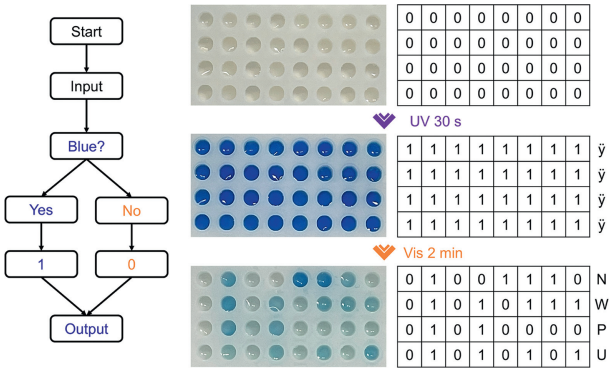


Fig. 5. Schematic illustration of the encryption and decryption process based on the WO_3 QDs and WO_3–CB[7] assembly.

diation with precise exposure time, which further empowers the anti-counterfeiting process with a higher security. Specifically, as shown in Fig. 5, by defining blue color of WO_3–CB[7] assembly and WO_3 QDs as "1" and their colorless state as "0", the initial state without UV irradiation provides invalid information with all sites in the array as "0". After about 30 s of UV light exposure, the ASCII binary encoded information "11 111 111" carried by the all-blue array can be read, which can be translated into "ÿÿÿÿ", yielding another error message. This confusing message will continuously show up until visible light is applied for 2 min, upon which all the sites containing WO_3 QDs become colorless and display the information of "0". In contrast, the WO_3–CB[7] solution retains blue, displaying the information of "1". Consequently, the true ASCII binary encoded information of "01 001 110", "01 010 111", "01 010 000" and "01 010 101" are acquired and translated into "N", "W", "P" and "U", respectively. Together, the genuine information of "NWPU" will be obtained. Notably, further extending the exposure time of visible light to 10 min will then lead WO_3–CB[7] composite to become colorless, resulting in invalid information. After that, the system becomes ready for a new encryption-decryption cycle. While a slight decrease in the contrast ratio occurred over 10 encryption-decryption cycles due to photochromic fatigue caused by electron transfer limitation [62], the maintained chromatic contrast between colorless and blue states still enables robust decryption performance. Thus, time-encoded anti-counterfeiting based on kinetics-tunable photochromic WO_3–CB[7] assembly was achieved, suggesting the effectiveness of the present system for the development of advanced anti-counterfeiting strategies.

To further extend the application of WO_3–CB[7] assembly, their potential use for fabricating information encryption devices was also evaluated through controllably depositing WO_3–CB[7] assembly into agarose hydrogels. As depicted in Fig. 6A, after UV irradiation for 30 s, hydrogels containing WO_3 QDs and WO_3–CB[7] assembly both turned blue with no significant color variation. Subsequently, continuous visible light irradiation was administered, leading to the anticipated fading of the blue hydrogels, which exhibited varying bleaching rates, in alignment with above findings in aqueous solution. Meanwhile, similar results were also obtained in hydrogels incorporated with competitive AD molecule, as illustrated in Fig. 6A.

Subsequently, time-encoded information encryption based on WO_3–CB[7] hydrogels was investigated. Typically, as shown in Fig. 6B, the strip-like agarose hydrogels of WO_3 QDs and WO_3–CB[7] assembly are spliced together, with an overhead cover of a black light-blocking plate with the word "IMPOSSIBLE" cut out. The "IM" portion is positioned above the WO_3 QDs hydrogel, while the "POSSIBLE" portion is above the WO_3–CB[7] hydrogel. When illuminated with a UV light, the cut-out "IMPOSSIBLE" section undergoes photochromism under the UV light and turns blue, while the rest of the hydrogel covered by the light-blocking plate retains unchanged. Consequently, the characters "IMPOSSIBLE" were displayed in the hydrogel after removing the light-blocking plate. When continuing to illuminate with visible light, the "IM" in the WO_3 QDs hydrogel fades gradually first (*ca.* 5 min) due to its faster photochromic rate compared to WO_3–CB[7] assembly, leaving only the "POSSIBLE" in the WO_3–CB[7] hydrogel. Upon further extending the visible light exposure for 8 min, the "POSSIBLE" also fades completely, achieving the erasure of the information. Thus, the process of making "IMPOSSIBLE" into "POSSIBLE", and finally nothing can be achieved through the present kinetic-tunable photochromic WO_3–CB[7] assembly. Apparently, the time-encoded response behaviors in hydrogels provide more complexity, which also holds great potential as patch-type flexible anti-counterfeiting materials on commodities.

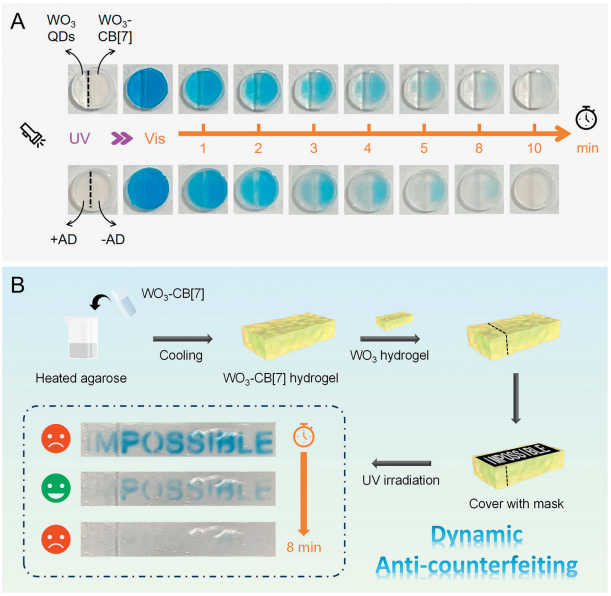


Fig. 6. (A) Top: photos of hydrogels containing WO_3 QDs (left) and WO_3–CB[7] assembly (right) before and after UV irradiation for 30 s and further light irradiation with visible light; Bottom: photos of hydrogels containing WO_3–CB[7] with (left) and without (right) AD before and after UV irradiation for 30 s and further light irradiation with visible light. (B) Schematic illustration of the encryption-decryption principle using different hydrogels based on WO_3–CB[7] assembly, and the photos of the WO_3 QDs/WO_3–CB[7] hydrogels for dynamic decryption to read the correct information.

In summary, we have developed WO_3 QD-based supramolecular assembly with tunable photochromic kinetics towards time-encoded anti-counterfeiting. Owing to the efficient suppression of absorbed water decomposition on WO_3 QDs by rigid and hydrophobic cavity of CB[7], kinetics-tunable photochromic property was successfully achieved, which can be precisely manipulated by simply adjusting the WO_3 QDs to CB[7] ratio. The fabricated WO_3–CB[7] assembly holds great potential for a variety of applications including time-resolved anti-counterfeiting and information encryption, thereby rendering it a promising candidate for developing novel intelligent optical materials. Compared with other photochromic anti-counterfeiting materials, the present photochromic supramolecular system possesses distinct time-encoded characteristic, with irradiation time serving as a pivotal parameter for decrypting the final information, further enhancing the complexity of replication and counterfeiting. Moreover, it is plausible to conceptualize the integration of other inorganic photochromic materials with diverse supramolecular entities *via* the present host-guest assembly approach to expand the scope of anti-counterfeiting materials.

Declaration of competing interest

The authors declare that they have no known competing financial interests or personal relationships that could have appeared to influence the work reported in this paper.

CRediT authorship contribution statement

Xiaojian Yan: Writing – original draft, Methodology, Investigation, Conceptualization. **Saijin Huang:** Methodology, Investigation. **Wenfeng Liu:** Investigation. **Li-Li Tan:** Methodology. **Gaobin Wang:** Methodology. **Liping Cao:** Methodology. **Li Shang:** Writing – review & editing, Supervision, Funding acquisition, Conceptualization.

Acknowledgments

This work is supported by the National Natural Science Foundation of China (No. 22274131), Shenzhen Science and Technology Program (Nos. JCYJ20220530161800001, JCYJ20240813150813018), and the Innovation Foundation for Doctor Dissertation of Northwestern Polytechnical University (No. #CX2024054). We would also like to thank the Analytical & Testing Center of Northwestern Polytechnical University for the testing and funding (No. 2024T017) support.

Supplementary materials

Supplementary material associated with this article can be found, in the online version, at doi:10.1016/j.cclet.2025.111427.

References

[1] Z.H. Zuo, Z.W. Feng, Y.Y. Peng, et al., ACS Nano 18 (2024) 4456–4466.
[2] A. Abdollahi, H. Roghani-Mamaqani, B. Razavi, Prog. Polym. Sci. 98 (2019) 101149.
[3] J.R. Otaegui, D. Ruiz-Molina, J. Hernando, C. Roscini, Adv. Funct. Mater. 34 (2024) 2402510.
[4] T. Lin, C. Tian, Y. Sun, et al., Chin. Chem. Lett. 34 (2023) 107864.
[5] B. Wu, M. Si, L. Hua, et al., Adv. Mater. 36 (2024) 2401659.
[6] A. Abdollahi, H. Roghani-Mamaqani, B. Razavi, M. Salami-Kalajahi, ACS Nano 14 (2020) 14417–14492.
[7] W. Zhong, L. Shang, Chem. Sci. 2024 (2024) 6218–6228.
[8] G. Liu, Y. Li, C. Tian, et al., Chin. Chem. Lett. 35 (2024) 109403.
[9] H. Li, X. Peng, W. Xi, et al., Adv. Funct. Mater. 34 (2024) 2405877.
[10] T. Chen, B. Xu, J. Han, et al., ACS Appl. Mater. Interfaces 16 (2024) 13305–13315.
[11] L. Wang, W. Zhong, W. Gao, W. Liu, L. Shang, Chem. Eng. J. 479 (2024) 147490.
[12] T. Zhang, X.Y. Lou, X. Li, et al., Adv. Mater. 35 (2023) 2210551.
[13] T. Wu, Y. Tian, J. Wu, et al., Dyes Pigment. 212 (2023) 111119.
[14] Z. Wang, Z. Ding, Y. Yang, et al., Chem. Eng. J. 457 (2023) 141293.
[15] H. Wang, J. Tang, H. Deng, et al., J. Mater. Chem. C 11 (2023) 15945–15951.
[16] X. Le, H. Shang, S. Wu, et al., Adv. Funct. Mater. 31 (2021) 2108365.
[17] J. Du, Z. Yang, H. Lin, D. Poelman, Responsive Mater. 2 (2024) e20240004.
[18] X. Dong, Y. Dang, Z. Wu, et al., Mater. Today Energy 44 (2024) 101632.
[19] A.B.A. Kayani, S. Kuriakose, M. Monshipouri, et al., Small. 17 (2021) 2100621.
[20] D. Wei, Y. Zhang, W. Xue, et al., ACS Sustain. Chem. Eng. 12 (2024) 6310–6319.
[21] B. Cui, G. Fu, Appl. Surf. Sci. 655 (2024) 159520.
[22] W. Si, S. Wang, Z. Yu, et al., Chem. Eng. J. 492 (2024) 152232.
[23] X. Yan, W. Zhong, S. Qu, Z. Li, L. Shang, J. Colloid Interface Sci. 646 (2023) 855–862.
[24] T. Chen, X. Mai, Y. Li, et al., Chem. Eng. J. 499 (2024) 155999.
[25] W. Tang, C. Zuo, C. Ma, et al., J. Mater. Chem. C 10 (2022) 18375–18384.
[26] S.W. Feng, X.L. Peng, J.J. Cui, et al., Adv. Funct. Mater. 34 (2024) 2401431.
[27] X. Zhang, R. Yang, Y. Dong, et al., Angew. Chem. Int. Ed. 63 (2024) e202403973.
[28] D. Das, P. Das, T. Das, et al., Angew. Chem. Int. Ed. (2024) e202414239.
[29] G. Zhao, Y. Kou, N. Song, et al., ACS Nano 17 (2023) 7624–7635.
[30] Y.Y. Gao, Y.H. Yang, Y.H. Wei, et al., Adv. Funct. Mater. (2024) 2416025.
[31] X. Yan, L. Wang, W. Zhong, et al., Nano Res. 18 (2025) 94907172.
[32] F. Tong, Y. Zhou, Y. Xu, et al., Exploration 3 (2023) 20210111.
[33] H. Yang, S. Li, J. Zheng, et al., Adv. Mater. 35 (2023) 2301300.
[34] Y. Zhang, Y. Ding, F. Lan, et al., Nanoscale 16 (2024) 21279–21293.
[35] S. Wang, W. Fan, Z. Liu, A. Yu, X. Jiang, J. Mater. Chem. C 6 (2018) 191–212.
[36] W. Meng, A.J.J. Kragt, X. Hu, et al., Adv. Funct. Mater. 34 (2024) 2402494.
[37] M. Chen, X. Zhang, W. Sun, et al., Nano Energy 123 (2024) 109352.
[38] W. Meng, A.J.J. Kragt, Y. Gao, et al., Adv. Mater. 36 (2023) 2304910.
[39] Y. Zhu, Y. Yao, Z. Chen, et al., Sol. Energ. Mat. Sol. C 239 (2022) 111664.
[40] Q. Liu, C. Hu, X. Wang, Appl. Surf. Sci. 480 (2019) 404–409.
[41] D. Kim, A. Aktalay, N. Jensen, et al., J. Am. Chem. Soc. 144 (2022) 14235–14247.
[42] W.L. Zhou, W. Lin, Y. Chen, X.Y. Dai, Y. Liu, Small 19 (2023) 2304009.
[43] B. Zhao, M. Wei, X. Zhou, et al., Adv. Funct. Mater. 35 (2025) 2416011.
[44] W. Zhong, X. Yan, S. Qu, L. Shang, Aggregate 4 (2023) e245.
[45] A. Syal, D. Sud, Sens. Actuator B: Chem. 266 (2018) 1–8.
[46] M.H. Gehlen, J. Photochem. Photobiol. C: Photochem. Rev. 42 (2020) 100338.
[47] L.L. Tan, M. Wei, L. Shang, Y.W. Yang, Adv. Funct. Mater. 31 (2021) 2007277.
[48] D. Li, Z.F. Feng, Y.J. Han, et al., Adv. Sci. 9 (2022) 2104790.
[49] Y.W. Li, Q.F. Li, X.R. Miao, et al., Angew. Chem. Int. Ed. 60 (2021) 6744–6751.
[50] Y.Z. Zhang, B. Zhou, Y.X. Liu, et al., J. Fluoresc. 18 (2008) 109–118.
[51] M. Li, R. Yang, X. Feng, et al., Food Hydrocoll. 127 (2022) 107506.
[52] S.B. Black, Y. Chang, C. Bae, M.A. Hickner, J. Phys. Chem. B 117 (2013) 16266–16274.
[53] Y. Huang, B. Wang, P. Lyu, et al., Nano Res. 16 (2023) 12165–12172.
[54] B.B. Cui, C.P. Guo, Z.H. Zhang, G.D. Fu, Chem. Eng. J. 455 (2023) 140822.
[55] K. Manalastas-Cantos, P.V. Konarev, N.R. Hajizadeh, et al., J. Appl. Crystallogr. 54 (2021) 343–355.
[56] X. Zuo, D.M. Tiede, J. Appl. Crystallogr. 57 (2024) 1446–1455.
[57] H. Liu, P.H. Zwart, J. Struct. Biol. 180 (2012) 226–234.
[58] J. Eberhardt, D. Santos-Martins, A.F. Tillack, S. Forli, J. Chem. Inf. Model. 61 (2021) 3891–3898.
[59] R.E. Rigsby, A.B. Parker, Biochem. Mol. Biol. Educ. 44 (2016) 433–437.
[60] J. Tian, L. Xia, J. Wu, et al., ACS Appl. Mater. Interfaces 12 (2020) 32352–32359.
[61] W. Zhao, B. Qiao, J. Tropp, et al., J. Am. Chem. Soc. 141 (2019) 4980–4989.
[62] S. Yamazaki, K. Isoyama, Langmuir 39 (2023) 10240–10248.